D. R. Lyons (Hampton University)
Fiber Optic Sensors Group

COMPREHENSIVE FINAL REPORT FOR THE PERIOD 4/97-4/99

"Fiber Optic Sensor Components and Systems For Smart Materials and Structures"

Final Report for NASA Grant NAG8-1340:

The general objective of the funded research effort has been the development of discrete and distributed fiber sensors and fiber optic centered opto-electronic networks for the intelligent monitoring of phenomena in various aerospace structures related to NASA Marshall specific applications. In particular, we have proposed and have been developing technologies that we believe to be readily transferable and which involve new fabrication techniques. The associated sensors developed can be incorporated into the matrix or on the surfaces of structures for the purpose of sensing stress, strain, temperature-both low and high, pressure field variations, phase changes, and the presence of various chemical constituents. These are the most significant milestones accomplished during the two-year funding period:

- We completed the fabrication and testing of the prototype unit for multiple sensor fabrication shown in Figure 1. This prototype consists of a high resolution, automated writing system composed of a double interferometer setup (one visible and the other UV). A schematic of the actual prototype is shown in Figure 2. This device will be used to register highly accurate and evenly spaced gratings in samples such as our D-fiber pressure sensors, ultra sensitive phase change detectors, shear stress monitors, and high density artificial (human oriented) nervous system. In order to test some of these concepts, we recently verified the ability to measure and write transverse holograms fibers with a priori knowledge of the resonances. This is an unparalleled accomplishment in this field. We have also, partly through Marshall funding, set up 4 high tech fiber optics laboratories with various diagnostic and fabrication capabilities. See laboratory photos in Figures 16-21.

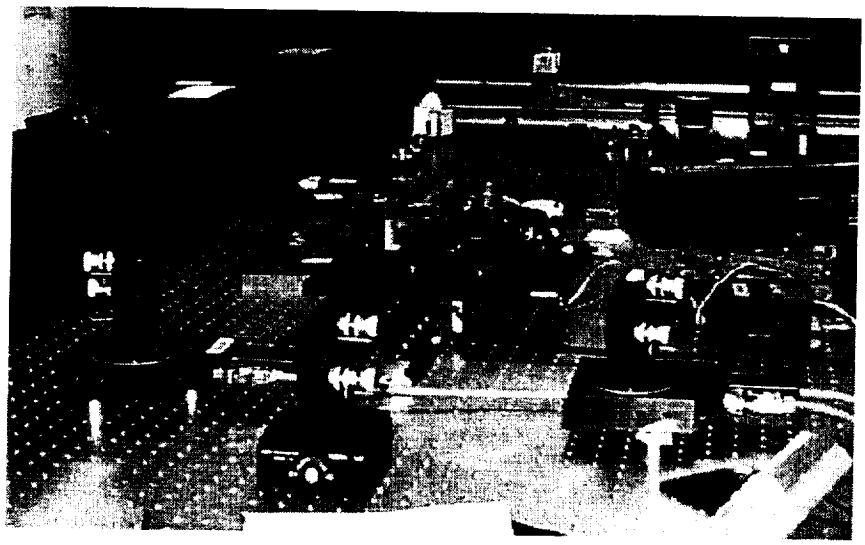

Figure 1. Prototype wavelength comparator for high resolution multi-sensor production.

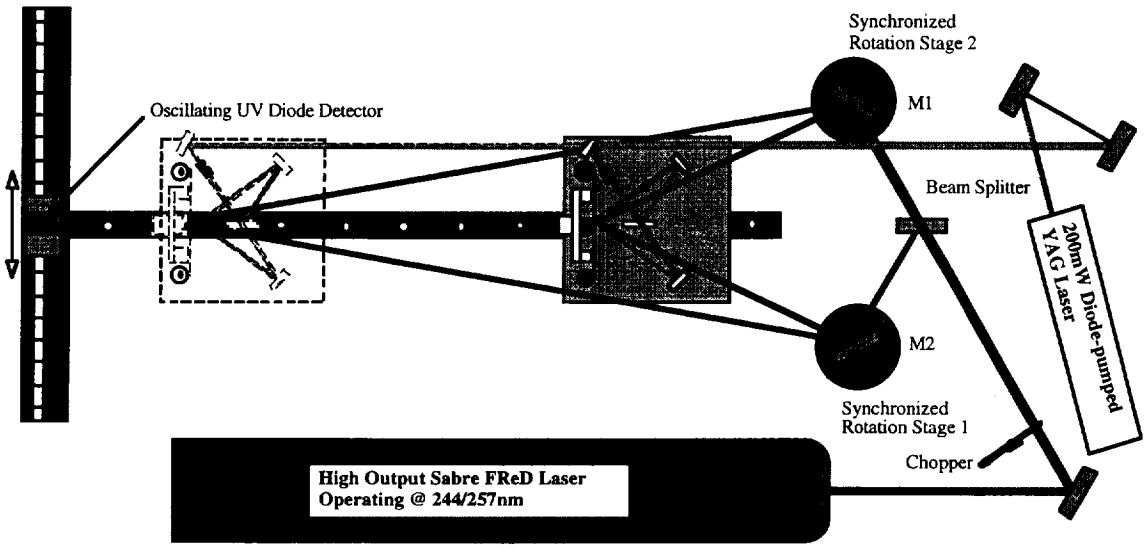

Figure 2. Double interferometer Bragg grating wavelength standard schematic layout.

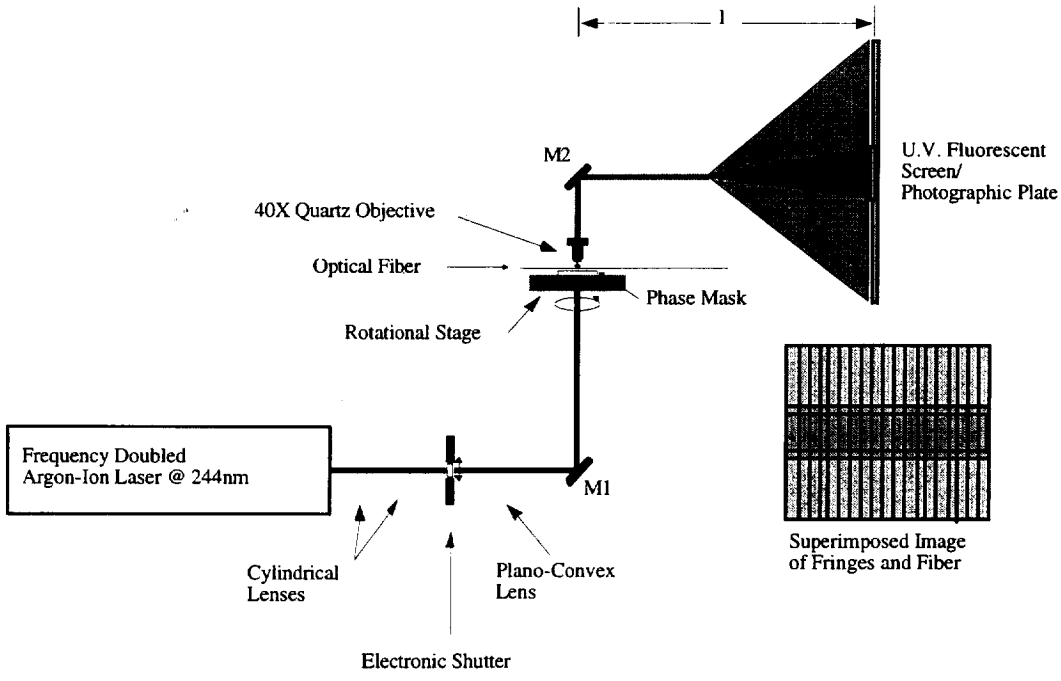

Figure 3. Bragg grating system used in phase mask defects and grating-fiber imaging work.

- Using D-type fibers and the photographic imaging techniques, we derived and filed a patent for an optimization algorithm for phase mask production. See 'Publications and Presentations' in Appendix A [1-3,11,12] and Scientific Patents and Patent Disclosures in Appendix B [1]. The consequences of this direction of research has been the design of a new tunable writing device and to a deeper understanding of the physics surrounding phase mask design and fabrication. See 'Patents and Disclosures' in Appendix B [2]. See Figure 5 for the principle of phase mask grating writing.

theoretical model that completely explains a certain class of typical anomalies in diffraction patterns produced certain commercial phase masks is the subject of a recently accepted paper entitled "Modeling and Observations of Phase Mask Trapezoidal Profiles Using Grating-Fiber Image Reproduction". The details of this model can be found in Appendix D.

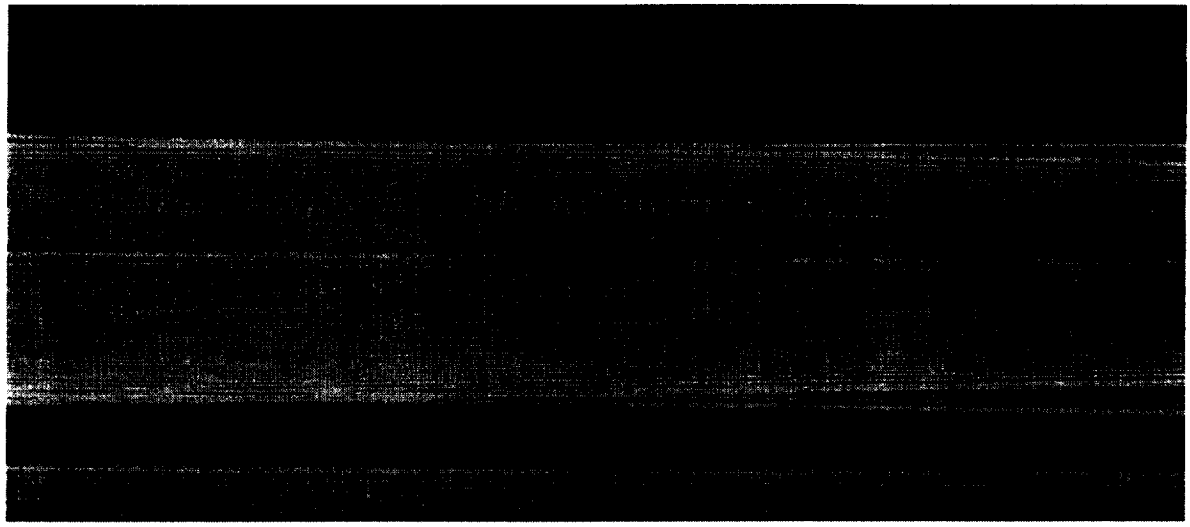

Figure 4. Image of UV fringes and D-fiber showing holographic grating patterns.

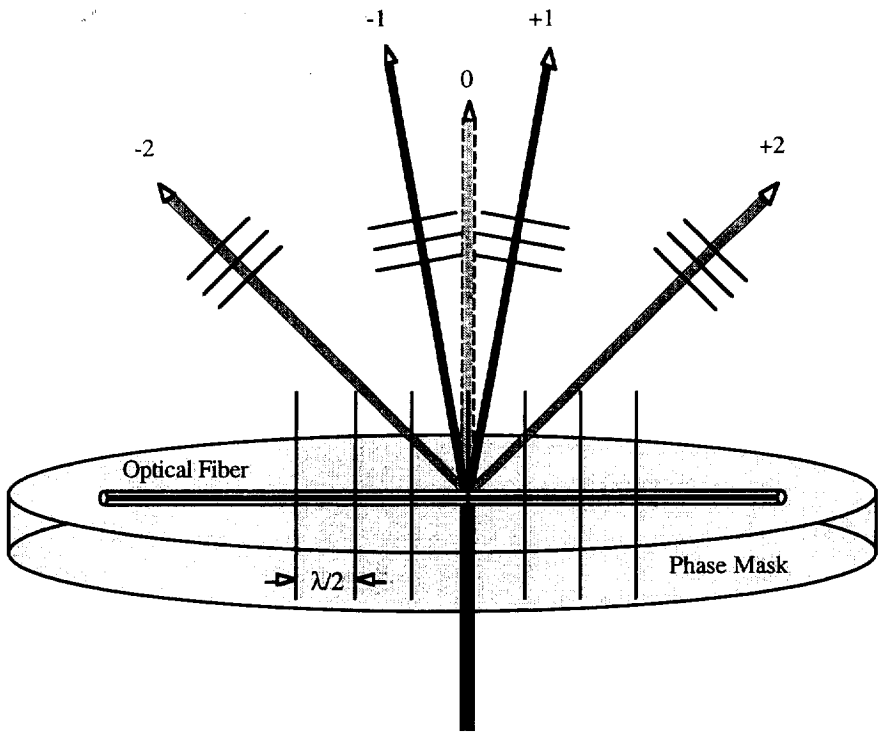

Figure 5. Illustration for optimization involving dominant first order beam diffraction.

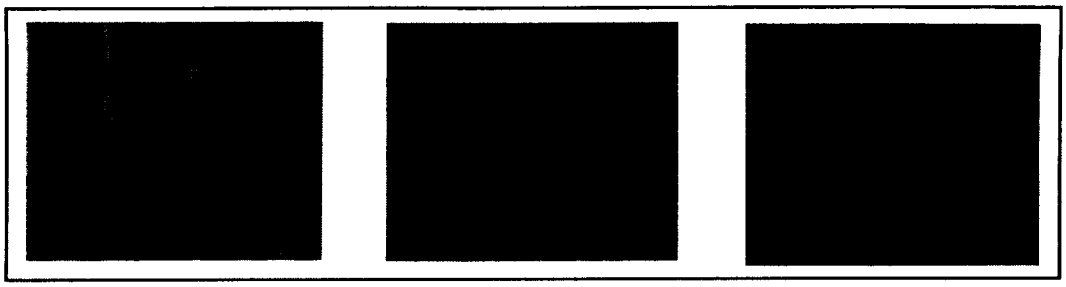

Figure 6. Phase Mask Period = 1.059μm | Phase Mask Period = 0.566μm | Transverse Holographic θ = 25 degrees

- The AFM images showing the two phase masks used in our paper entitled "Modeling and Observations of Phase Mask.Trapezoidal Profiles.Using..." are included for completeness. See Appendix A [11] and Figure 7. These images were then fitted to our model to mathematically generate the fringes of Figure 8. Note the striking similarities.

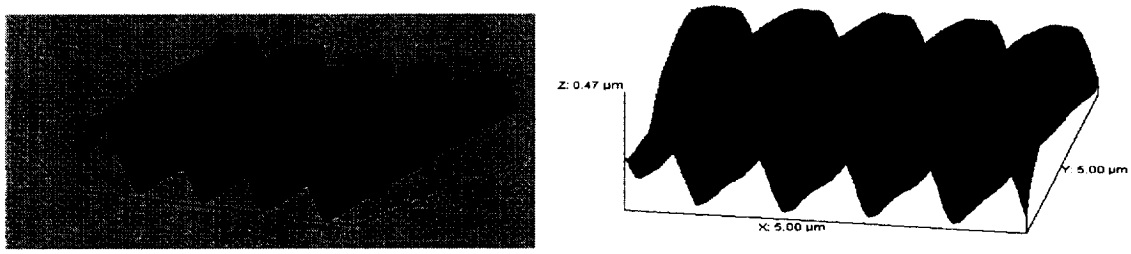

Figure 7. AFM Images of .566μm and 1.059μm Phase Masks

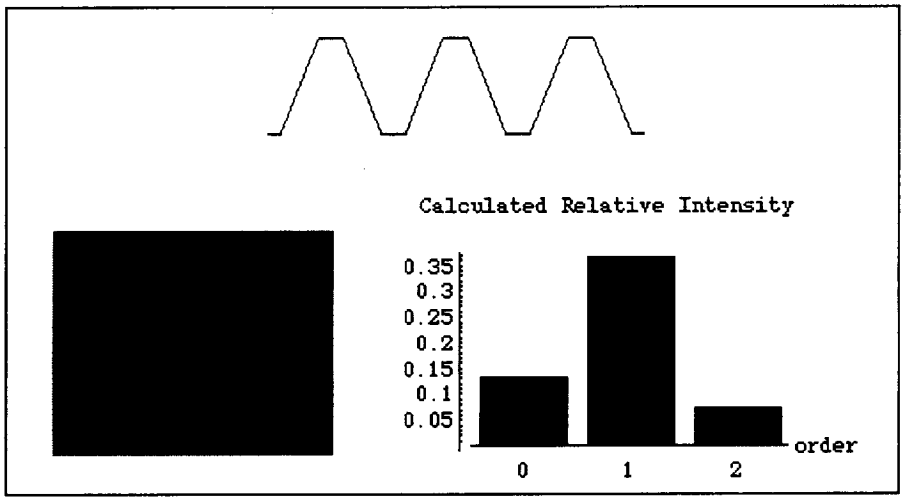

Figure 8. Trapezoidal phase mask pattern for .566μm mask and corresponding Mathematica fringe pattern.

- The fiber optic shear stress monitor mentioned at the end of last year's report was also built and tested. It produced very promising results in that we were able to directly correlate wavelength shifts in our sensor due to stress. These shifts are indicators of both wind speed and the stress in a structure resulting from these shearing forces. We produced several designs for optical fiber wind shear sensor one of that uses D-fibers with Bragg gratings embedded into structural surfaces. It incorporates compressed air flowing across a surface containing a matched pair sensor unit, whose modulated twin unit is outside of the region being measured, shear forces then generate a modulated error signal when incorporated into a phased locked system. Although the technical complexity of this experiment extended beyond the scope of this research grant, the work is still currently being partially funded under another NASA grant. In addition, a recent experimental setup along with a conceptual design for an evanescent-field pressure and phase change sensor are shown in Figures 9 and 10.

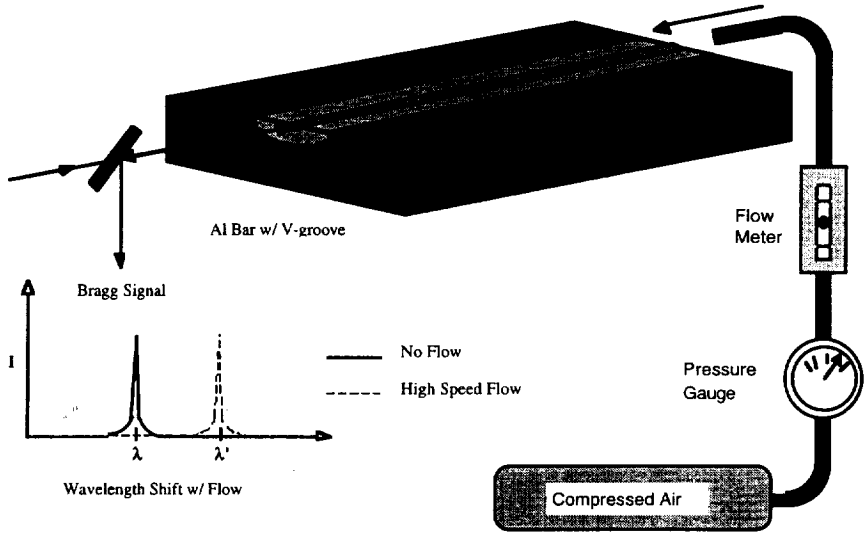

Figure 9. Shear Stress Experimental Setup

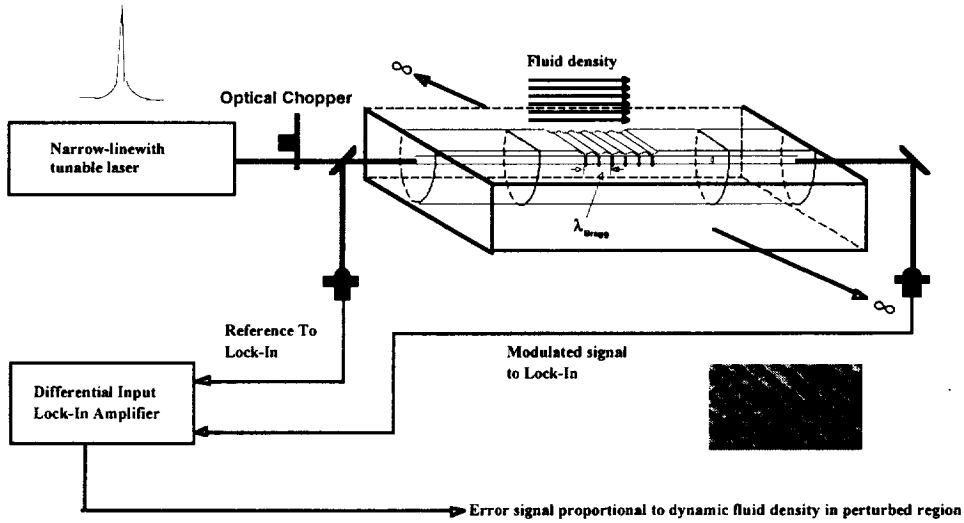

Figure 10. Evanescent field pressure sensor that could detect the invisible presence of ice on aircraft wings

- We have experimentally demonstrated that these sensors have reasonable responses and sensitivities. We also have a number of new designs for optimizing the response of these sensors for various configurations. Sensitivity enhancements also include the choice of retrofit materials in which the sensors are embedded, amplification of the strain transfer to the D-fiber sensors using gradation of material, and Bragg wavemeteer produced evanescent field coupling for ultra-sensitive operation. In addition, we will continue low priority work, begun during this grant, on the development of a miniature FO spectrum analyzer for readout verification and characterization of distributed Bragg filters within a given fiber unit. This verification method involves the device shown in Figure 11 along with its response to a single frequency, actively stabilized He-Ne laser. Figure 12 shows the our conceptual design of the resulting SMFOSA unit that is to be used for Bragg filter characterization. The motivation for this endeavor is to deliver compact readouts along with grating units to NASA centers that have interest in them.

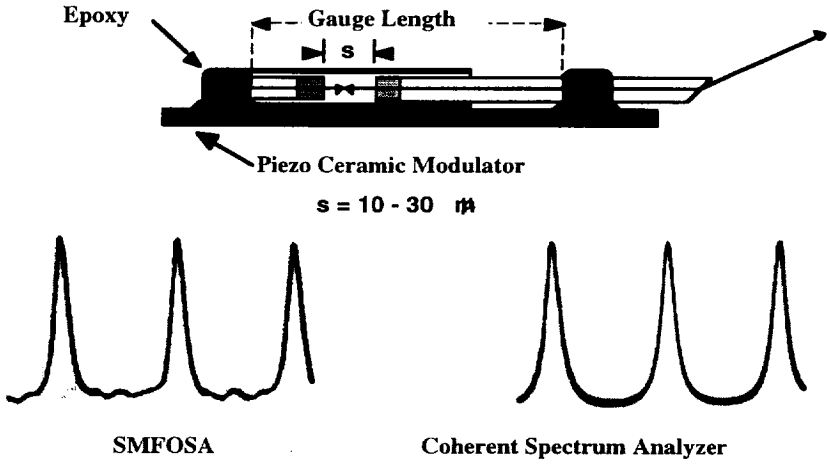

Figure 11. Single mode fiber optic spectrum analyzer for use as a compact Bragg grating readout.

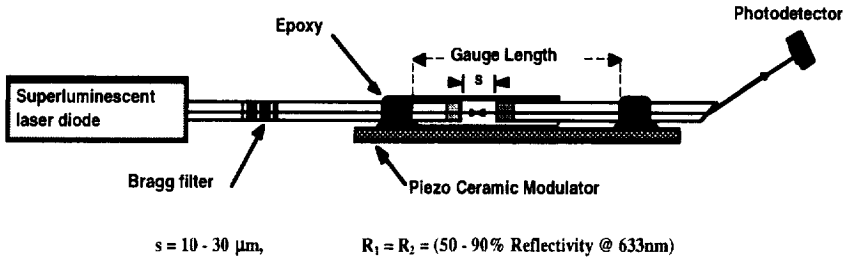

Figure 12. Bragg grating detection using in-house constructed SMFOSA.

- Figures 13 and 14 show the experimental diagram of our Ti:Sapphire laser system used for grating characterization and a typical Bragg resonance which it was used to detect. This system has been used as a narrow linewidth source and we expect it to remain an invaluable resource in the future with respect to the continuance of certain of the project

- objectives. An additional tunable diode laser for Bragg filter characterization was purchased, in part through the funding supplied under NAG8-1340.

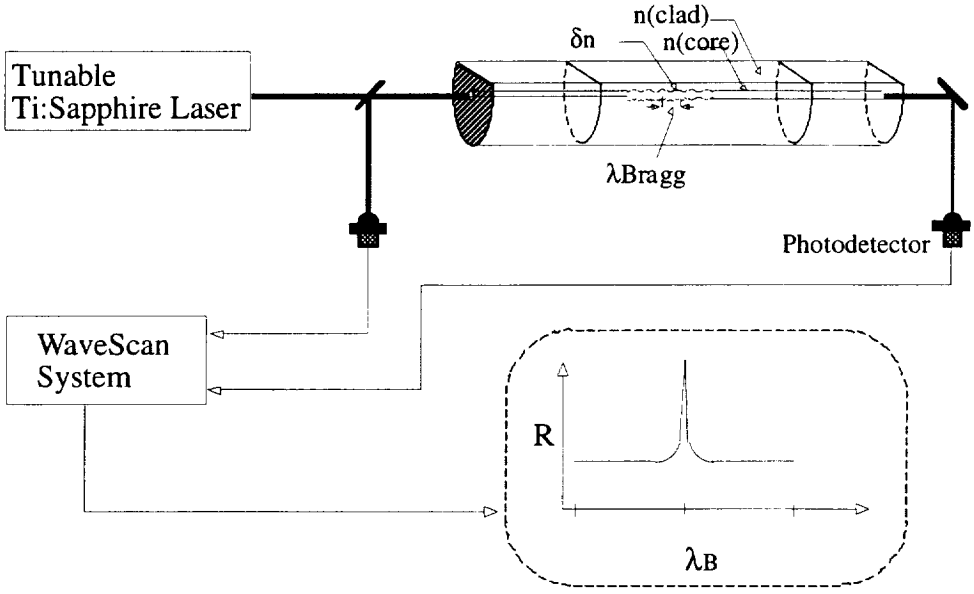

Figure 13. Tunable laser scanning system for D-fiber gratings using a Ti:Sapphire laser.

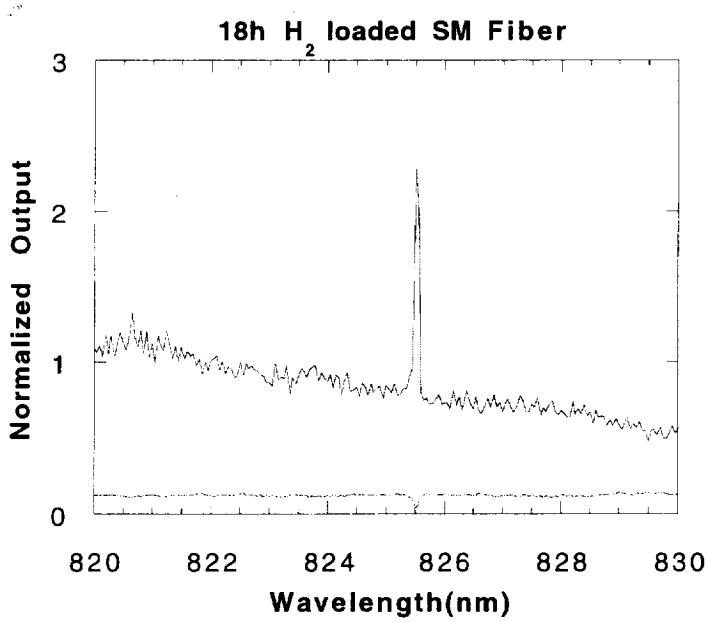

Figure 14. Output from Ti:Sapphire scanning laser system.

- Finally, our laboratory has continued the development fiber optic sensing devices based upon the simple Fabry-Perot design depicted in figure 15.

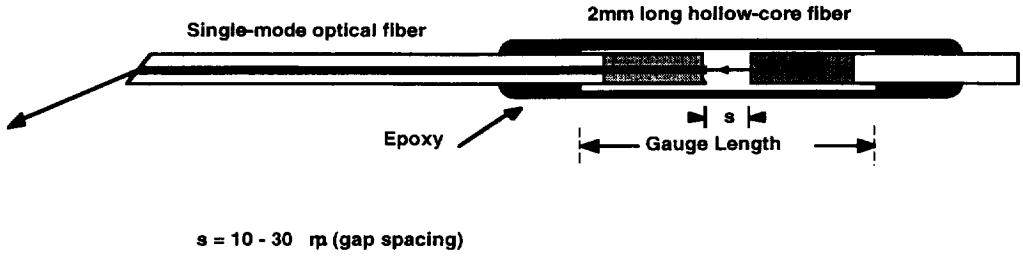

Figure 15. Single mode fiber optic Fabry-Perot sensor routinely fabricated in our laboratories.

Laboratory Resources Made Available in Part or Whole Due to NAG8-1340 Funding:

The following photos show portions of the laboratories and some of the experimental setups including the computer controlled Ti:Sapphire laser system used for high resolution characterization of Bragg grating sensors (Figure 16), the Coherent commercial spectrum analyzer system used as a standard for comparison to the first experimental trace shown in Figure 11 (Figure 17), our new multi-displinary fiber optic sensors laboratory (Figure 18), the Northrop-Grumman Fiber Optic Sensors Lab originally donated to Hampton University in 1993 (Figure 19) with an AFM setup (Figure 20), members of the Fiber Optic Sensors and Smart Structures Group (Figures 21 and 22), and the wavemeter Development Group (Figure 23).

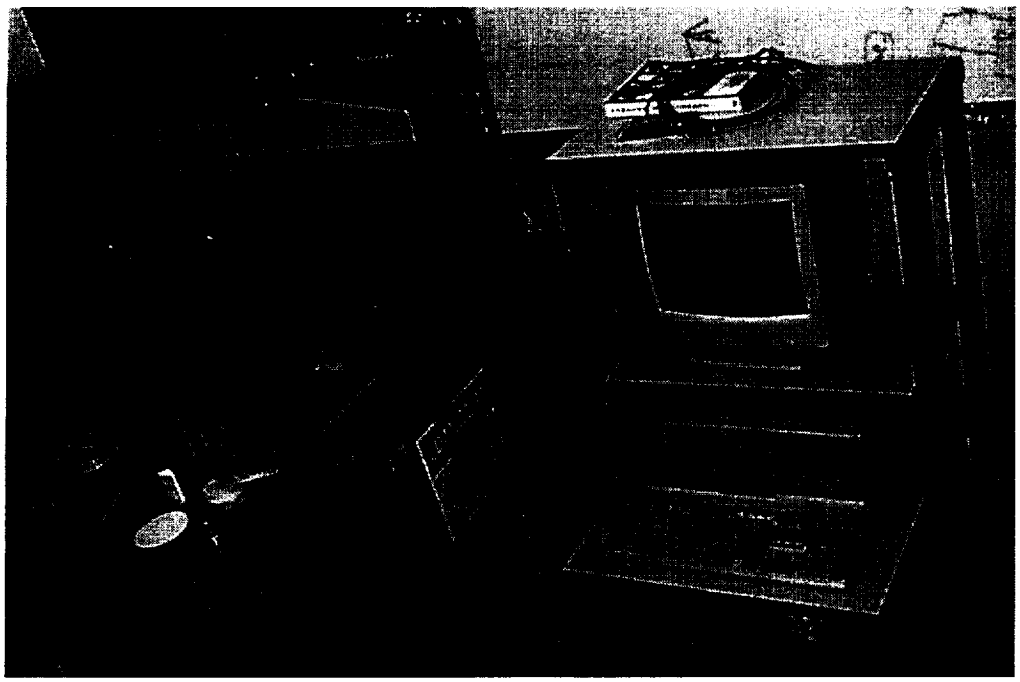

Figure 16. A Tunable Ti:Sapphire laser system with WAVESCAN used for Bragg grating diagnostics.

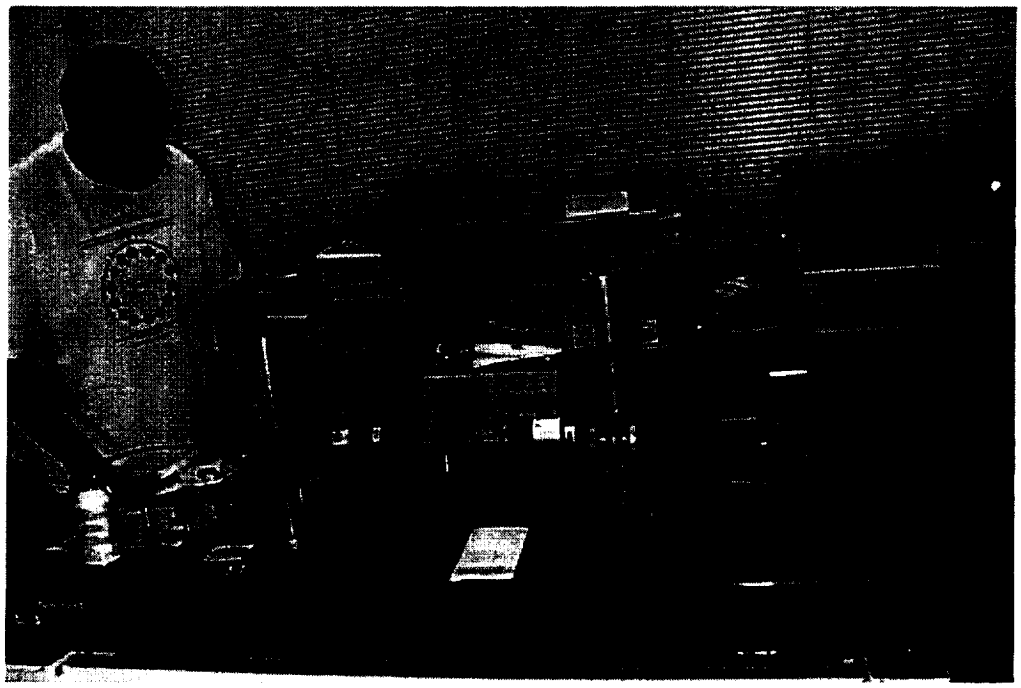

Figure 17. Coherent, Inc. commercial spectrum analyzer used to evaluate the SMFOSA in Figure 9a.

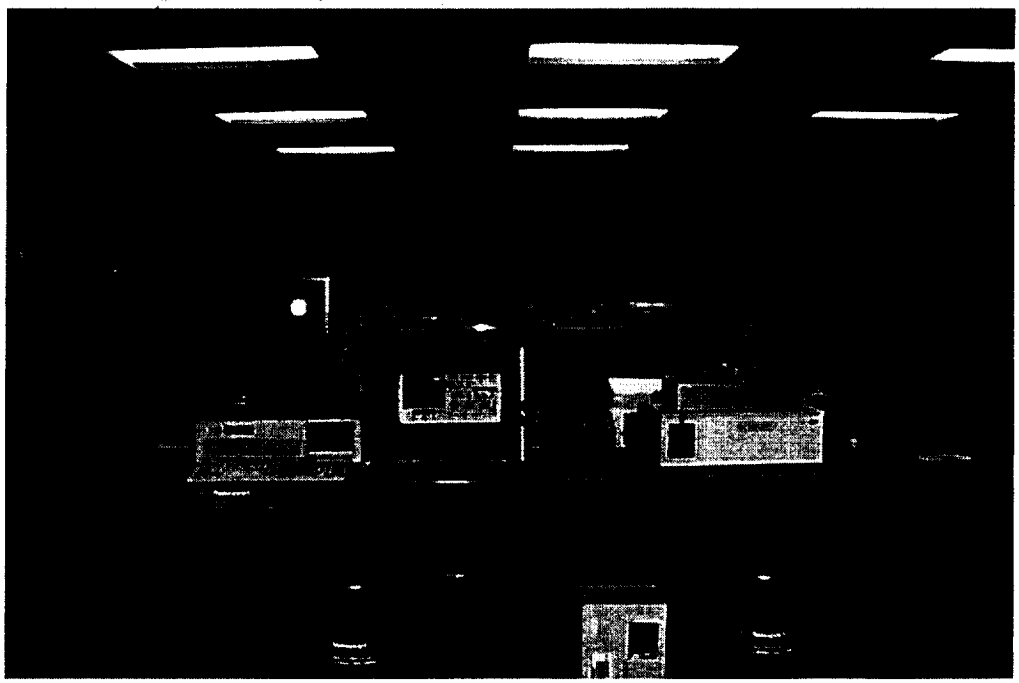

Figure 18. New multidisplinary fiber optic sensors laboratory where distributed sensor writing device is located along with other grating diagnostics.

Figure 19. Northrop-Grumman Fiber Optic Sensors Laboratory originally donated in 1993.

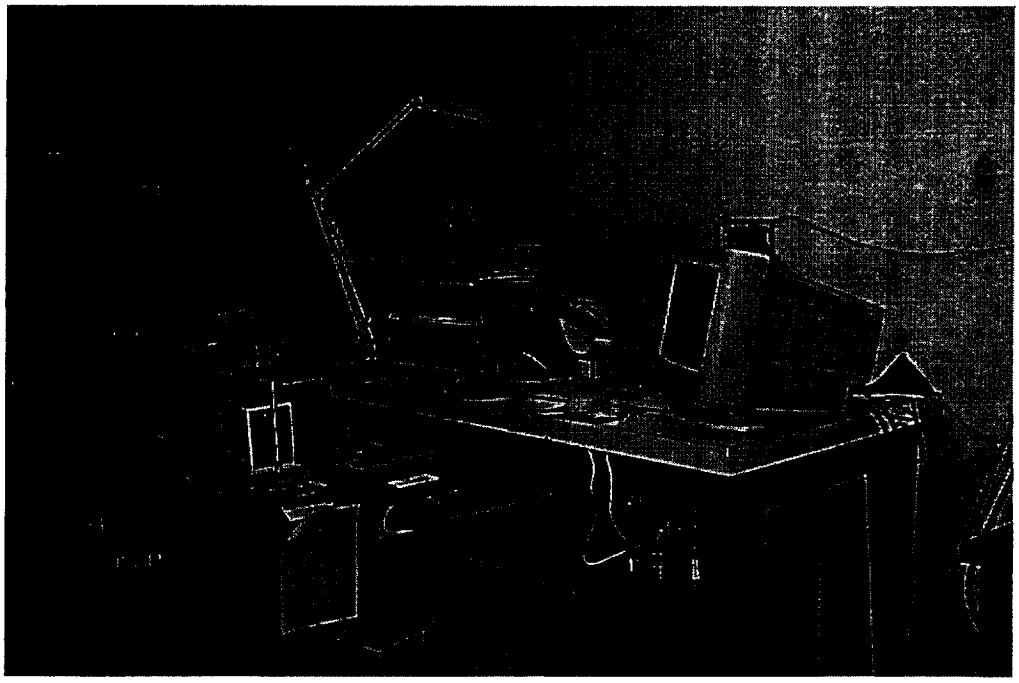

Figure 20. The atomic force microscope used to generate images in phase mask defects work.

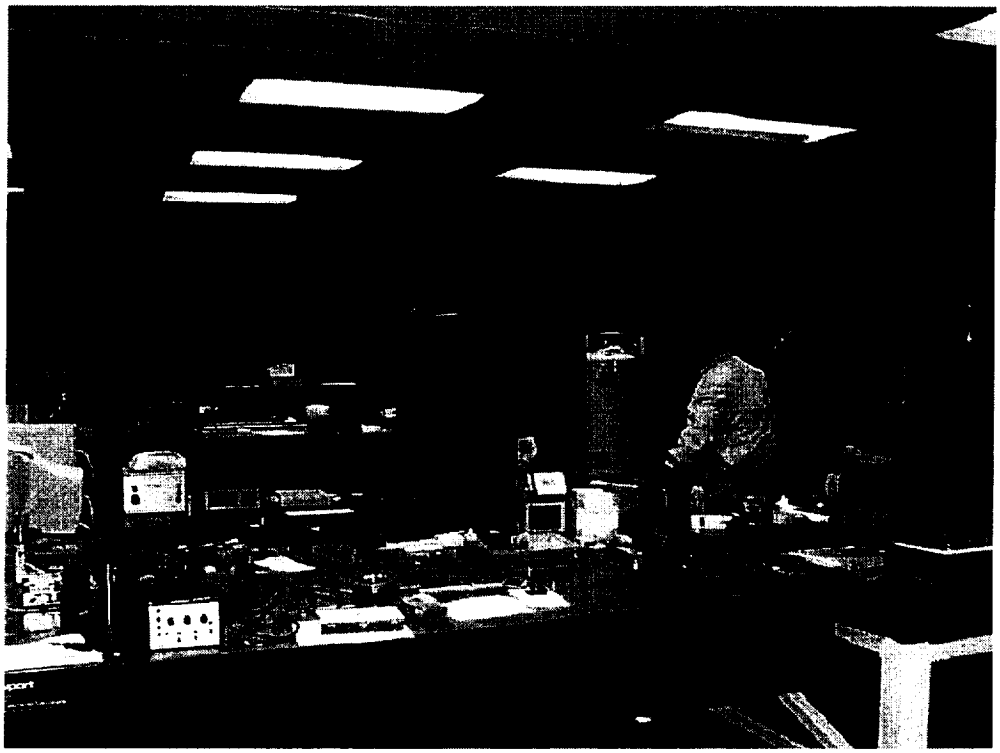

Figure 21. Senior graduate student and visiting professor working in multi-disciplinary laboratory

Figure 22. Fiber Optic Sensors and Smart Structures Group

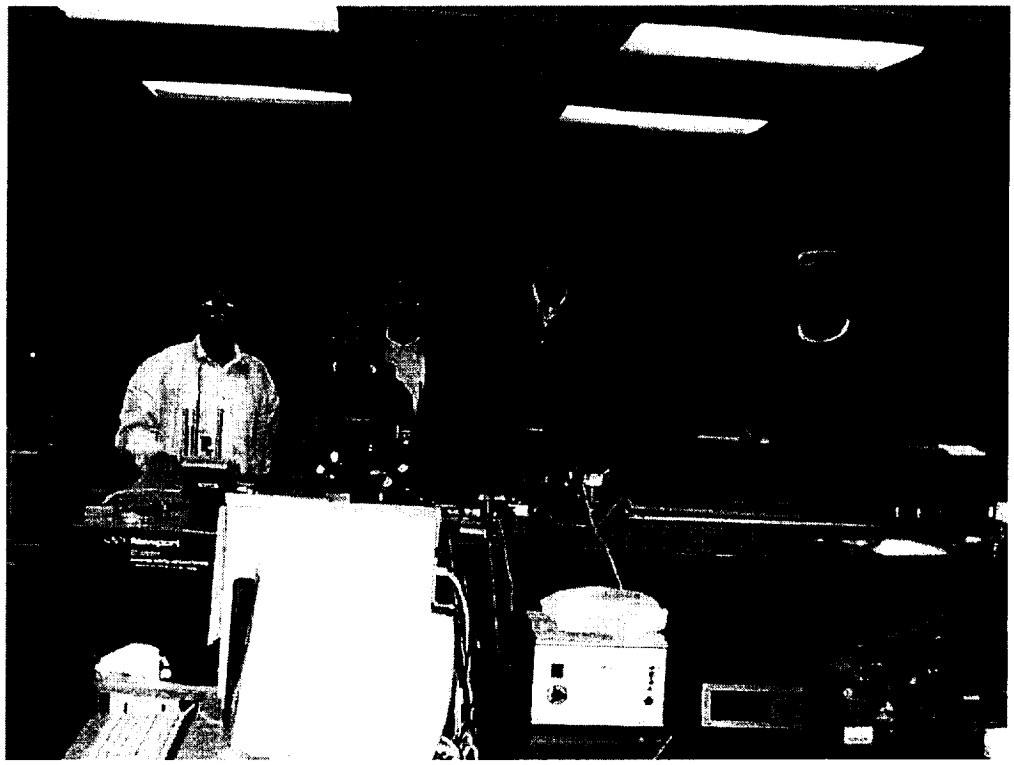

Figure 23. Fiber Bragg grating wavemeter development team

Finally, see Appendix C for a list of the students who have participated in research activities related to NASA Grant NAG8-1340 as either partially funded or non-funded student researchers.

Appendix A

Publications and Presentations Referenced to NASA grant NAG8-1340

1. H.R. Lee and D.R. Lyons, "Image Reproduction of Bragg Gratings", Proc. SPIE, Vol. 2778,p. 157 (1996).

2. D.R. Lyons, "Grating-Fiber Image Reproduction Technique for Bragg Reflection Filters", Fourth Annual HBCUs Research Conference, NASA Lewis Research Center, April 9-10, 1997.

3. D.R. Lyons, "Observations of Phase Mask Defects Using Grating-Fiber Imaging Techniques", Fourth Annual HBCUs Research Conference, NASA Lewis Research Center, April 9-10, 1997.

4. D.R. Lyons, "Novel Architectures for Intelligent Artificial Limbs using Embedded 2-D and 3-D Wavelength Multiplexed Optical Waveguides", Private Briefing to Chief of the Rehabilitation Medicine Branch of NIH, April 23,1997.

5. Yu. L. Grishkin, et al., "Preliminary Study of a Gas Microstrip Chamber on a Sapphire Substrate", Nuclear Instruments and Methods in Physics Research A, 354 (1995) 309-317, Yu. L. Grishkin, et al.

6. E.D. Brass and D.R. Lyons, "An Analytical Description of Phase Mask Defects as Verified by Grating-Fiber Image Reproduction", Fifth Annual HBCUs Research Conference, NASA Lewis Research Center, April 8-9, 1998.

7. K. Samuel and D.R. Lyons, "Preliminary Fringe-Counting Verification for a Bragg Grating Wavelength Standard", Fifth Annual HBCUs Research Conference, NASA Lewis Research Center, April 8-9, 1998.

8. E.J. Thompson and D.R. Lyons, "UV Induced Densification and Ablation During the Formation of Bragg Gratings in SiO_2 Preforms, Optical Fibers, and Gradient Index Lenses", Fifth Annual HBCUs Research Conference, NASA Lewis Research Center, April 8-9, 1998.

9. M.M. Khet and D.R. Lyons, "Theoretical Formulations Towards the Solution of Radiation Loss Problems in Optical Waveguide Couplers with Selectable Power Splitting Ratios", Fifth Annual HBCUs Research Conference, NASA Lewis Research Center, April 8-9, 1998.

10. D. R. Lyons, "Fiber Optic Sensing Technologies Developed at Hampton University", Sensors EXPO Conference, Cleveland, OH, September 14, 1999.

11. D.R. Lyons, J.V. Lindesay, Z. Ndlela, H.R. Lee, and E.J. Thompson, "Modeling and Observations of Phase Mask Trapezoidal Profiles Using Grating-Fiber Image Reproduction", Accepted for Publication in Applied Optics (November 1999).

12. E.J. Thompson, E.D. Brass, K. Samuel, S. Ray Bullock, J. Lindesay, and D.R. Lyons, "The Formation of Phase Gratings on the End of Gradient Index (GRIN) Lenses Using UV Ablation at 193nm", Published in Applied Optics (November 1, 1999).

Appendix B

Scientific Patents and Patent Disclosures Associated with NASA Grant NAG8-1340

1. Defects Minimization Process for the Fabrication of Optical Phase Masks Used in Fiber Bragg Grating Production, **Disclosure**, Filed October 6, 1997, J.V. Lindesay and D.R. Lyons.

2. Wavelength Tunable Phase Mask for Writing Bragg Reflection Filters, Disclosure, Filed May 20, 1999, D.R. Lyons and J.V. Lindesay.

3. Non-Intrusive Fiber Optic Sensor for Detection of Lead in Environmental and Biological Systems, **Disclosure**, Filed Sept. 30, 1997, D.R. Lyons and S.R. Bullock.

4. High Temperature Fiber Optic Sensor, **Disclosure**, Filed Mar. 20, 1997, D.R. Lyons and J.V. Lindesay.

5. Instrumented Patch for Repair of Fatigue Damaged or Sensitive Structure, **United States Patent Number_P-5,553,504**, Sept. 10, 1996, D.R. Lyons, S.M. Reich; P. Shyprykevich.

6. Methods of and Apparatus for Calibrating Precisely Spaced Multiple Transverse Holographic Gratings in Optical Fibers, **United States Patent Number_P-5,552,882**, Sept. 3, 1996, D.R. Lyons; Z. U. Ndlela.

7. An Evanescent Field-Based, Non-Intrusive, Fiber Optic Hydrodynamic Fluid Sensor, Filed April 26, 1997, D.R. Lyons and J. V. Lindesay.

Appendix C

Students Associated with Work Done on NASA Grant NAG8-1340

Ph.D. Thesis Advisor to:

a. Mr. Hyung Lee	(Not Funded Under Grant)	**Graduated**
b. Mr. Kenneth Samuel	(Partially Funded Under Grant)	**Graduating**
c. Mr. Eric Brass	(Partially Funded Under Grant)	**Current**
d. Ms. Erica Thompson	(Partially Funded Under Grant)	**Current**
e. Ms. Myat Khet	(Not Funded Under Grant)	**Graduating**

M.S. Thesis Advisor to:

f. Ms. Carramah Quiett	(Partially Funded Under Grant)	**Current**

As a Research Advisor to the following undergraduate students, I provided individual research projects and guided each student to the completion of their project relating to NASA Grant NAG8-1340.

a. Ms. LaRuth Pendergrass	E.E.	**Graduated**
b. Ms. Tosha Hudson	Physics	**Graduated**
c. Ms. Chekesha Clingman	Physics	**Graduated**

Guided Summer Research Assistant:

a. Ms. Millen W. Gabreselassie	**Graduated**

As a Research Advisor to the following high school students, I provided individual research projects and guided each student to completion of their project relating to NASA Grant NAG8-1340.

a. Mr. Daniel Lee	**Sharp Plus**
b. Ms. Rina Lau	**Sharp Plus**

Appendix D

Phase Mask Defects Theory Derived Under NASA Grants for Fiber Sensor Development

The periodic grating structure of the simplest phase mask design has the general shape of a rectangular wave pattern, having an amplitude of **h** and a spatial period (pitch) of **b+a** which consists of the barrier width **b** of the pattern and separation spacing **a** (See Fig. 1(a)). In contrast, the grating structure of the phase masks examined has the general shape of a symmetric trapezoidal wave pattern, having amplitude **h´** with varying slopes (See Fig. 1(b)).

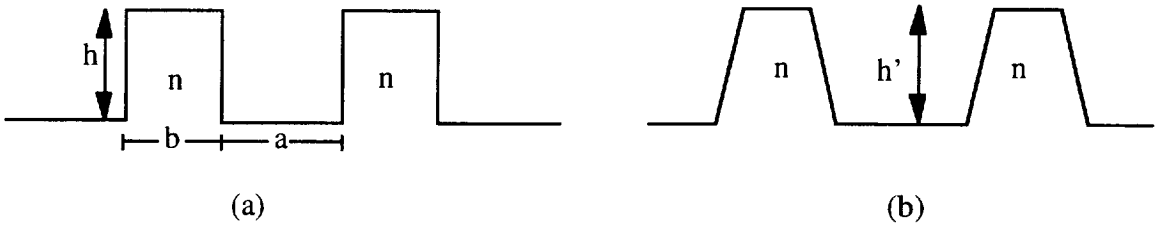

Fig. 1. (a) Schematic of ideal phase mask of spatial period b+a and amplitude h (b) trapezoidal structure used to model general defects and reproduce observed UV fringe pattern

For certain choices of the spatial pattern, the phase mask can be designed such that the zeroth order diffracted beam is suppressed considerably relative to the first order beams (See Fig. 4a in body). In these cases, the principal order emerging from the phase mask will be the two first order beams. In the usual design of a phase mask which has negligible zeroth order, the pattern is assumed to be rectangular with spacing between barriers set equal to barrier widths and the height chosen such that the optical path length difference for paths within the barrier vs. paths outside (at normal incidence) is one-half wavelength. However, to more accurately describe the diffraction obtained for such spatial patterns, the paths shown in Fig. 2 were examined for light incident upon the phase mask.

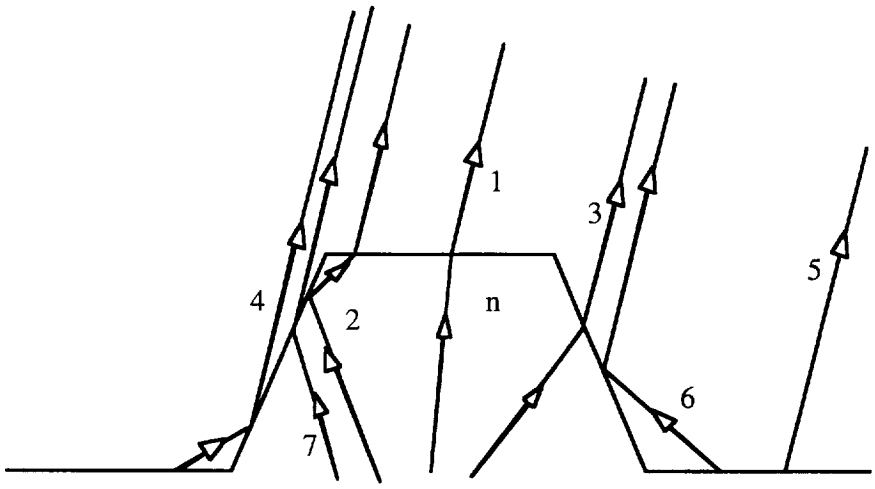

Fig. 2. Trapezoidal grating structure showing the paths examined to describe the diffraction pattern

Appendix D (Continued)

In the usual design, only the paths 1 and 5 are considered for a rectangular grating. The contributions from all seven paths can be summed and superposed to generate the diffraction amplitude. The necessary equation is obtained from basic diffraction theory and is given by,

$$\psi(\varphi) = \sum_{paths} \int_{j\ path\ limits} A_j(\varphi)\exp(ik\Delta l_j(x,\varphi))dx$$

Eq. (1)

where the optical path lengths Δl_j can be calculated using Snell's law and geometric parameters, and the amplitudes A_j are the transmission and reflection amplitudes corresponding to the incident polarization state for each beam.

The ray amplitudes A_j depend upon the transmission and reflection fields at a planar interface, obtained directly from the optical boundary conditions, given by the following expressions for polarizations:

$$T_p = \frac{2\cos(\varphi_{in})\sin(\varphi_{out})}{\sin(\varphi_{in}+\varphi_{out})}$$

$$R_p = \frac{-\sin(\varphi_{in}-\varphi_{out})}{\sin(\varphi_{in}+\varphi_{out})}$$

$$T_t = \frac{2\cos(\varphi_{in})\sin(\varphi_{out})}{\sin(\varphi_{in}+\varphi_{out})\cos(\varphi_{in}-\varphi_{out})}$$

$$R_t = \frac{\tan(\varphi_{in}-\varphi_{out})}{\tan(\varphi_{in}+\varphi_{out})}$$

Eq. (2)

Appendix D (Continued)

In the above expressions, p indicates polarization perpendicular to the plane of incidence of wave vectors, whereas t indicates that the polarization is in the same plane as the wave vectors.

Each of the various ray paths in Fig. 2 will involve different geometrical factors, especially those paths that contact the sides of the trapezoid. Calculation of the point of contact of a ray will require the following factors, which give the coordinates of the contact:

$$\xi_{left}(x,\varphi) = (x\tan(\vartheta_s) + b\tan\varphi)/(\tan(\vartheta_s) - \tan\varphi)$$

$$\xi_{right}(x,\varphi) = (x\tan(\vartheta_s) + b\tan\varphi)/(\tan(\vartheta_s) + \tan\varphi)$$

$$y_{left}(x,\varphi) = \Theta(\vartheta_s)(b + \xi_{left}(x,\varphi))\cot(\vartheta_s) + (1 - \Theta(\vartheta_s))(\xi_{left}(x,\varphi) - x)\cot\varphi$$

$$y_{right}(x,\varphi) = \Theta(\vartheta_s)(b - \xi_{left}(x,\varphi))\cot(\vartheta_s) + (1 - \Theta(\vartheta_s))(\xi_{left}(x,\varphi) - x)\cot\varphi$$

Eq. (3)

Given these geometrical factors, the amplitudes A_j, optical path lengths Δl_j, and limits of integration can be directly determined, and are given below for each path of Figure 2:

$$A_1 = T(\varphi_{in},\varphi_{out})$$

$$\Delta l_1 = nh\sec(\varphi_{in}) + (a - h\tan(\varphi_{in}) - x)\sin(\varphi_{out})$$

$$n\sin\varphi_{in} = \sin\varphi_{out}$$

$$Max[-b,-(a + h\tan(\varphi_{in}))] \le x \le a - \tan(\varphi_{in})$$

$$A_2 = R(\pi/2 - \vartheta_s + \varphi_{2in})T(\varphi_{in},\varphi_{out})$$

$$\Delta l_2 = y_2\sec(\varphi_{2in}) + n(h - y_2)\sec(\varphi_{2in}) + (a - x_2 - (h - y_2)\tan(\varphi_{in}))\sin(\varphi_{out})$$

$$\varphi_{2in} = 2\vartheta_s - \varphi_{in}$$

$$x_2 = \xi_{left}(x,\varphi_{2in})$$

$$y_2 = y_{left}(x,\varphi_{2in})$$

$$-b \le x \le Min[-(a + h\tan(\varphi_{2in})),b]$$

Appendix D (Continued)

$$A_3 = T(\pi/2 - \vartheta_s - \varphi_{3in}, \pi/2 - \vartheta_s - \varphi_{out})$$

$$\Delta l_3 = n y_3 \sec(\varphi_{3in}) + (x_3 - a)\cos(\varphi_{out} + \vartheta_s)/\sin(\vartheta_s)$$

$$\varphi_{3in} = \arccos(\cos(\varphi_{out} + \vartheta_s)/n) - \vartheta_s$$

$$x_3 = \xi_{right}(x, \varphi_{3in})$$

$$y_3 = y_{right}(x, \varphi_{3in})$$

$$Max[-b, a - h\tan\varphi_{3in}] \le x \le b$$

$$A_4 = R(\pi/2 - \vartheta_s + \varphi_{out})T(\varphi_4, \varphi_{4in})$$

$$\Delta l_4 = y_4 \sec(\varphi_{4in}) + (h - y_4)\cos(\varphi_{out}) - (x_4 - a)\sin(\varphi_{out})$$

$$\varphi_{4in} = 2\vartheta_s - \varphi_{out}$$

$$n\sin\varphi_4 = \sin\varphi_{4in}$$

$$x_4 = \xi_{left}(x, \varphi_{4in})$$

$$Max[b - 2w, -a - h\tan\varphi_{4in}] \le x \le -b$$

$$A_5 = T(\varphi_{in}, \varphi_{out})$$

$$\Delta l_5 = (a - x)\sin(\varphi_{out}) + h\cos(\varphi_{out})$$

$$-w \le x \le -b\Theta(\vartheta_s - \varphi_{out}) - (a + h\tan\varphi_{out})\Theta(\varphi_{out} - \vartheta_s)$$

$$b \le x \le Min[w, 2w - a - h\tan\varphi_{out}]$$

$$A_6 = R(\pi/2 - \vartheta_s - \varphi_{out})T(\varphi_6, \varphi_{6in})$$

$$\Delta l_6 = y_6 \sec(\varphi_{6in}) + (x_6 - a)\cos(\varphi_{out} + \vartheta_s)/\sin(\vartheta_s)$$

Appendix D (Continued)

$$\varphi_{6in} = -(2\vartheta_s + \varphi_{out})$$

$$x_6 = \xi_{right}(x, \varphi_{6in})$$

$$y_6 = y_{right}(x, \varphi_{6in})$$

$$b \le x \le Min[a - h\tan\varphi_{6in}, 2w - b]$$

$$A_7 = T(\pi/2 - \vartheta_s + \varphi_{7in}, \pi/2 - \vartheta_s + \varphi_{out})$$

$$\Delta l_7 = n y_7 \sec(\varphi_{7in}) + (h - y_7)\cos(\varphi_{out}) - (x_7 - a)\sin(\varphi_{out})$$

$$\varphi_{7in} = \vartheta_s - \arccos(\cos(\vartheta_s - \varphi_{out})/n)$$

$$x_7 = \xi_{left}(x, \varphi_{7in})$$

$$y_7 = y_{left}(x, \varphi_{7in})$$

$$-b \le x \le Min[-(a + h\tan\varphi_{7in}), b]$$

Eq. (4)

The diffracted beams combine in this plane to create a Bragg interference pattern for the two polarization types satisfying the form

$$|\Psi_{pBragg}(x,z)|^2 = \left|\int_{all} \psi(\varphi)\exp(ikz\cos\varphi)\cos(k(2a-x)\sin\varphi)d\varphi\right|^2$$

$$|\Psi_{tBragg}(x,z)|^2 = \left|\int_{all} \psi(\varphi)\exp(ikz\cos\varphi)\cos\varphi\cos(k(2a-x)\sin\varphi)d\varphi\right|^2 +$$

$$\left|\int_{all} i\psi(\varphi)\exp(ikz\cos\varphi)\sin\varphi\sin(k(2a-x)\sin\varphi)d\varphi\right|^2$$

Eq. (5)

The predominant contribution to this integral will be due to the narrow interference peaks of the contributing orders if the number of pattern repetitions is large.